Research Article | Vol. 25, No. 3 | 6 Feb 2017 | OPTICS EXPRESS 2422

Optics EXPRESS

Fully integrated microwave frequency synthesizer on heterogeneous silicon-III/V

JARED HULME,[1,*] MJ KENNEDY,[1] RUI-LIN CHAO,[1,2] LINJUN LIANG,[1,3] TIN KOMLJENOVIC,[1] JIN-WEI SHI,[1,2] BOGDAN SZAFRANIEC,[4] DOUG BANEY,[4] AND J. E. BOWERS[1]

[1]*Electrical and Computer Engineering Department, University of California Santa Barbara, California, USA*
[2]*Department of Electrical Engineering, National Central University, Jungli, Taiwan*
[3]*Institute of Lightwave Technology, Beijing Jiaotong University, Beijing, China*
[4]*Keysight Technologies, Santa Clara, California, USA*
[*]*jaredhulme@ece.ucsb.edu*

Abstract: We demonstrate a photonic microwave generator on the heterogeneous silicon-InP platform. Waveguide photodiodes with a 3 dB bandwidth of 65 GHz and 0.4 A/W responsivity are integrated with lasers that tune over 42 nm with less than 150 kHz linewidth. Microwave signal generation from 1 to 112 GHz is achieved.

OCIS codes: (140.5960) Semiconductor lasers; (230.5160) Photodetectors; (250.5300) Photonic integrated circuits.

References and links

1. S. Ohmori, Y. Yamao, and N. Nakajima, "The Future Generations of Mobile Communications Based on Broadband Access Technologies," IEEE Commun. Mag. **38**(12), 134–142 (2000).
2. S. Koenig, D. Lopez-Diaz, J. Antes, F. Boes, R. Henneberger, A. Leuther, A. Tessmann, R. Schmogrow, D. Hillerkuss, R. Palmer, T. Zwick, C. Koos, W. Freude, O. Ambacher, J. Leuthold, and I. Kallfass, "Wireless sub-THz communication system with high data rate," Nat. Photonics **7**(12), 977–981 (2013).
3. J.-W. Shi, C.-B. Huang, and C.-L. Pan, "Millimeter-wave Photonic Wireless Links for Very-High Data Rate Communication," NPG Asia Mater. **3**(2), 41–48 (2011).
4. H.-J. Song and T. Nagatsuma, "Present and Future Terahertz Communications," IEEE Trans. Terahertz Sci. Technol. **1**(1), 256–263 (2011).
5. A. Stöhr, S. Babiel, P. J. Cannard, B. Charbonnier, F. van Dijk, S. Fedderwitz, D. Moodie, L. Pavlovic, L. Ponnampalam, C. C. Renaud, D. Rogers, V. Rymanov, A. J. Seeds, A. G. Steffan, A. Umbach, and M. Weiß, "Millimeter-Wave Photonic Components for Broadband Wireless Systems," IEEE Trans. Microw. Theory Tech. **58**(11), 3071–3082 (2010).
6. A. W. Fang, H. Park, O. Cohen, R. Jones, M. J. Paniccia, and J. E. Bowers, "Electrically pumped hybrid AlGaInAs-silicon evanescent laser," Opt. Express **14**(20), 9203–9210 (2006).
7. L. A. Coldren and S. W. Corzine, *Diode Lasers and Photonic Integrated Circuits,* (John Wiley & Sons, 1995), Chap. 4.
8. K. Kato, "Ultrawide-Band/High-Frequency Photodetectors," IEEE Trans. Microw. Theory Tech. **47**(7), 1265–1281 (1999).
9. X. Xie, Q. Zhou, E. Norberg, M. Jacob-Mitos, Y. Chen, Z. Yang, A. Ramaswamy, G. Fish, J. C. Campbell, and A. Beling, "High-Power and High-Speed Heterogeneously Integrated Waveguide-Coupled Photodiodes on Silicon-on-Insulator," J. Lightwave Technol. **34**(1), 73–78 (2016).
10. J.-M. Wun, H.-Y. Liu, Y.-L. Zeng, S.-D. Yang, C.-L. Pan, C.-B. Huang, and J.-W. Shi, "Photonic High-Power Continuous Wave THz-Wave Generation by Using Flip-Chip Packaged Uni-Traveling Carrier Photodiodes and a Femtosecond Optical Pulse Generator," J. Lightwave Technol. **34**(4), 1387–1397 (2016).
11. A. Beling, H.-G. Bach, G. G. Mekonnen, R. Kunkel, and D. Schmidt, "Miniaturized waveguide-integrated p-i-n photodetector with 120-GHz bandwidth and high responsivity," IEEE Photonics Technol. Lett. **17**(10), 2152–2154 (2005).
12. Y. Chung, D.-G. Kim, and N. Dagli, "Reflection properties of coupled-ring reflectors," J. Lightwave Technol. **24**(4), 1865–1874 (2006).
13. S. Srinivasan, M. Davenport, T. Komljenovic, J. Hulme, D. T. Spencer, and J. E. Bowers, "Coupled Ring Resonator Mirror Based Heterogeneous III-V Silicon Tunable Laser," IEEE Photonics J. **7**(3), 1–8 (2015).
14. T. Komljenovic, M. Davenport, J. Hulme, A. Liu, C. Santis, A. Spott, S. Srinivasan, E. Stanton, C. Zhang, and J. E. Bowers, "Heterogeneous Silicon Photonic Integrated Circuits," J. Lightwave Technol. **34**(1), 20–35 (2016).
15. T. Komljenovic, M. Davenport, S. Srinivasan, J. Hulme, and J. E. Bowers, "Narrow linewidth tunable laser using coupled resonator mirrors," presented at the OFC., Los Angeles, CA, USA, Paper W2A.52 (2015).

#279613 https://doi.org/10.1364/OE.25.002422
Journal © 2017 Received 7 Nov 2016; revised 30 Dec 2016; accepted 31 Dec 2016; published 31 Jan 2017

Optics EXPRESS

16. T. Okoshi, K. Kikuchi, and A. Nakayama, "Novel method for high resolution measurement of laser output spectrum," Electron. Lett. **16**(16), 630–631 (1980).
17. J. Hulme, J.Shi, M. J. Kennedy, T. Komljenovic, B. Szafraniec, D.Baney, R. Chao, and J. E. Bowers, "Fully integrated heterodyne microwave generation on heterogeneous silicon-III/V," accepted by MWP conference (2016).
18. G. Carpintero, K. Balakier, Z. Yang, R. C. Guzm'an, A. Corradi, A. Jimenez, G. Kervella, M. J. Fice, M. Lamponi, M. Chitoui, F. van Dijk, C. C. Renaud, A. Wonfor, E. A. J. M. Bente, R. V. Penty, I. H. White, and A. J. Seeds, "Microwave Photonic Integrated Circuits for Millimeter-Wave Wireless Communications," J. Lightwave Technol. **32**(20), 3495–3501 (2014).
19. T. Komljenovic, S. Srinivasan, E. Norberg, M. Davenport, G. Fish, and J. E. Bowers, "Widely Tunable Narrow-Linewidth monolithically integrated external-cavity semiconductor lasers," IEEE J. Sel. Top. Quantum Electron. **21**(6), 214–222 (2015).

1. Introduction

There is an urgent need to increase data capacity to prepare for the projected demands of wireless access services [1]. Millimeter-wave-over-Fiber (MoF) communication systems [2–4] are considered one of the best options to satisfy those demands. The final mile of these systems utilize remote antenna units (RAU) [1] in which integrated lasers, modulators, and high-speed photodiodes are key elements [5]. The use of heterogeneous silicon-III/V technology to integrate all the essential optical-to-electrical (O-E) and electrical-to-optical (E-O) components on one chip is an effective way to reduce the size, cost, and energy consumption of these RAUs.

In this study we demonstrate a novel heterogeneously integrated silicon-InP photonic microwave generator. An important element is the integration of the high-speed photodiode to be used in this system. A 3 dB bandwidth of 65 GHz and a reasonable internal responsivity of 0.4 A/W are achieved. At 70 GHz operating frequency, the measured saturation current is as high as 9 mA.

We also explore two types of tunable laser used in this chip. Wavelength tuning up to 42 nm and laser linewidths below 150 kHz are demonstrated.

Finally, a fully-integrated microwave generator chip combining both laser and photodiode is discussed. The outputs from two tunable lasers are beat on a fast photodetector to generate variable frequency microwave signals. The conceptual chip schematic is shown in Fig. 1. Signal generation from DC up to 112 GHz is demonstrated, showing that the heterogeneous silicon-InP platform is a viable option for RAU in MoF systems.

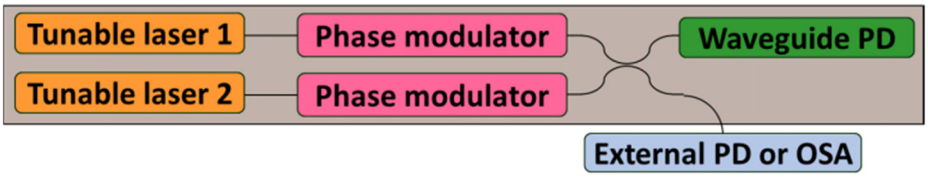

Fig. 1. Schematic diagram of the photonic microwave generator chip.

2. Fabrication

Rib waveguides were fully etched in 500 nm thick silicon-on-insulator (SOI) with 1 μm of buried oxide. The III/V was bonded directly to the silicon in the process described by [6] to allow evanescent coupling into the quantum well and PD absorber regions. Three distinct InP stacks were bonded to the SOI to be used for gain, modulator, and photodiode sections. These were designed to allow them to be co-processed to reduce the number of steps.

3. Photodiode structures and measurement

Figure 2(a) shows a conceptual cross-section of the photodiode (PD). Figure 2(b) shows a schematic of the top-view of the SOI waveguides. The waveguide width is tapered to gradually couple the optical power from the SOI waveguide to upper III-V active layers. The active region is overlaid in green and also represents the size of the p-contact layer. The length of the

Optics EXPRESS

final 0.6 μm waveguide and the width of the active region (w) are not specified in the figure because two different sizes of III-V active PD were fabricated. The device active area ($w \times l$) for devices A and B is 120 (4×30) and 45 (3×15) μm^2, respectively. Figure 2(c) shows an SEM image of the PD, where the SOI waveguide is buried below thick (~3.5 μm) dielectric layers (oxide and BCB) and cannot be seen. The thick dielectric is used to reduce the parasitic capacitance of the device from probe pads. Figure 3(a) shows the measured dark I-V curve for both devices. Both show clear rectifying behavior with low dark currents (10 nA at –2 V bias for 120 μm^2). Also, although device B has a smaller active area, it exhibits a larger dark current than that of A. This implies that the dark current in these devices mainly originates from surface state induced leakage current, which is proportional to the perimeter to volume ratio, rather than from bulk defects in the III-V material [7].

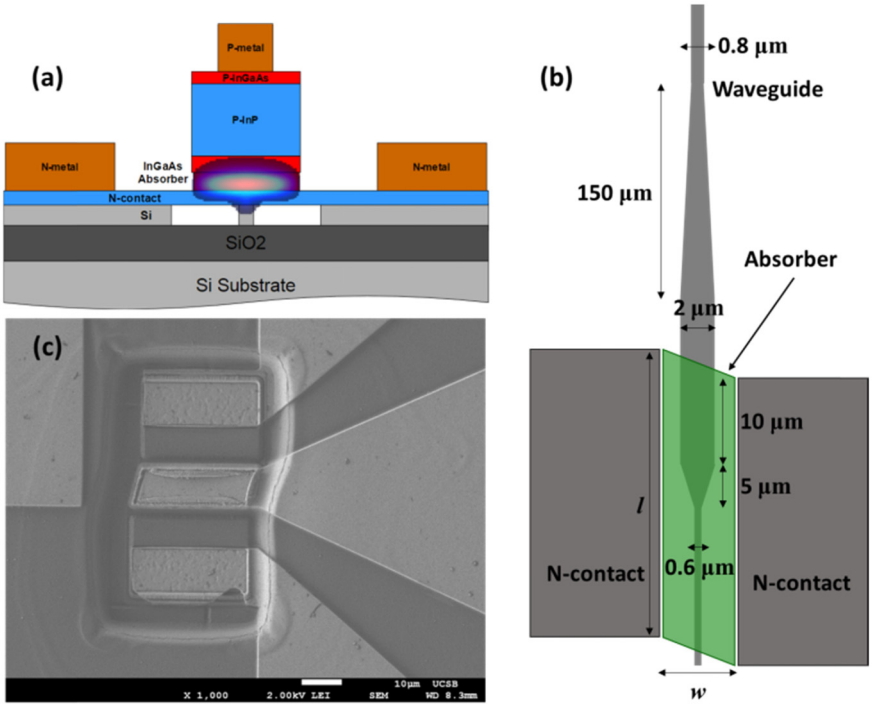

Fig. 2. (a) Conceptual cross-sectional view of fabricated PD with mode simulation overlay. (b) Conceptual top-view of fabricated PD. (c) SEM picture of top-view of fabricated PD.

Figure 3(b) shows the simulated distribution of the optical power in the direction of wave propagation. As shown in Fig. 2(a), the III-V active region is composed of p-i-n PD structure with a 400 nm intrinsic $In_{0.53}Ga_{0.47}As$ absorption layer and InP cladding layers. The simulation [Fig. 3 (b)] shows that the launched optical power from the input facet can be almost completely absorbed within the 30 μm device length. This indicates that device A should have a higher responsivity than device B due to its longer active region. After de-embedding the wavelength dependent facet coupling loss (~10 dB), the extracted DC internal responsivity of devices A and B is around 0.4 and 0.25 A/W, respectively, as shown in Fig. 3(c). Both traces show a broad optical window greater than 100 nm. PD measurements were performed at 23 °C. It should be noted that the facets for these devices were located near each other on the test bar, so variations in facet loss should be minimal.

The measured bias dependent O-E frequency response under low (1 mA) and high (3 mA) output photocurrents for device A can be seen in Fig. 4. From near dc (100 MHz) to 67 GHz, this measurement is taken with a lightwave component analyzer (Agilent, N4373 D). For

Optics EXPRESS

measurement beyond 67 GHz, the setup was changed to a two-laser heterodyne-beating system. The photo-generated MMW power was measured with an E-band (60-90 GHz) power sensor (Keysight, E8486A) and MMW waveguide probe (GGB, Model 90). For lower output photocurrent (1mA), the measured 3-dB O-E bandwidth of device A under −5 V is close to 65 GHz. However, for 3 mA output photocurrent it is clear that a high reverse bias voltage (−5V) is necessary to maintain the same 3-dB O-E bandwidth performance at 65 GHz. This indicates that the higher reverse bias voltage is necessary to compensate for the speed degradation induced by the space-charge screening (SCS) effect, which is usually observed in high-speed PDs under high-power operation [8]. Also, under a low reverse bias (−1 V), the photodiode ceases to work beyond low frequency operation. This is attributed to a more pronounced SCS effect and the insufficient depletion of the $In_{0.53}Ga_{0.47}As$ absorption layer under such a small reverse bias.

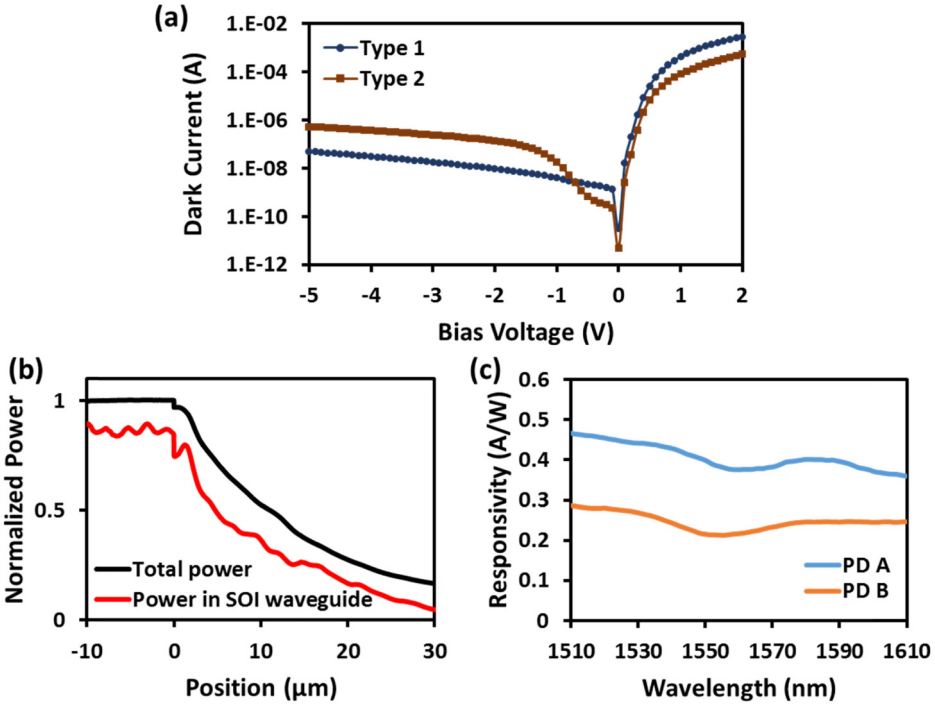

Fig. 3. (a) Measured internal responsivity of PDs under −3V bias vs. wavelength. (b) Measured dark current of fabricated PDs. (c) The simulated optical power along the direction of wave propagation.

The parasitic and junction capacitances usually result in an RC-limited speed performance of high-speed PDs on Si [9]. One way to reduce the RC time constant is to decrease the active area of the PD. This was done by fabricating device B which has a much smaller active area than device A (45 vs. 120 μm^2). Figure 5 shows the measured O-E frequency response under 1 mA output photocurrent and different voltage biases for device B. In spite of the difference in active area, the 3-dB O-E bandwidth for device B is very close to that of device A (67 vs. 65 GHz). This implies that the RC-limited bandwidth is not the dominant limiting factor in the net O-E bandwidth of the PDs demonstrated here.

Optics EXPRESS

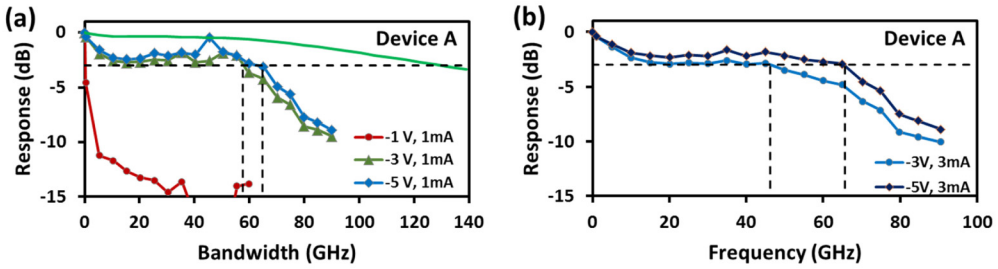

Fig. 4. Measured O-E frequency response of device A under (a) 1 mA and (b) 3 mA output photocurrent for different biases. The solid green line on (a) represents the extracted RC-limited frequency response at 1 mA.

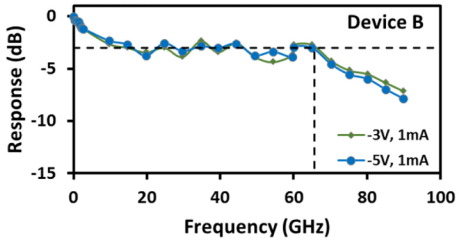

Fig. 5. Measured O-E frequency response of device B under 1 mA output photocurrent for different biases.

To achieve a more clear understanding of the relationship between the O-E bandwidth roll-off, the RC limitations and the carrier transit time, an equivalent circuit model was created for the PD A. The RC-limited bandwidth (f_{RC}) was extracted using the measured microwave reflection coefficients (S_{11}) of the photodiode [10]. Figure 6 shows the adopted equivalent circuit model used for the fitting of the measured S_{11} parameters. The extracted values of all circuit elements except R_T and C_T are included in a table, as well as a Smith chart with the measured and fitted S_{11} curves. C_J and R_J are the junction capacitance and resistance, respectively. R_C represents the differential resistance of the active diode. C_P is the parasitic capacitance induced by the probe-pad co-planar waveguide configuration. R_P and L_P represent the ohmic loss and inductance, respectively, of these metal lines. R_G and C_G are the dielectric loss and capacitance from the dielectric layer (BCB and SiO_2) below the probe metal. VCCS signifies voltage-controlled source. The PAD simulation blocks used included the parasitic effects of the co-planar waveguide. These parameters were calculated using momentum simulation software (HFSS).

To extract f_{RC} from the photodiode model, the elements R_T and C_T were removed, as these are used to model the low-pass frequency response of the internal carrier transit time [10]. The fitted curve in Fig. 6(b) matches the measured fairly well for PD A from near DC to 67 GHz, but the fitting of the smaller Type 2 PD proved difficult. The extracted RC-limited frequency response for PD A is shown in Fig. 4(a) in green and exhibits a 3 dB roll-off at 133 GHz. Comparing the extracted RC-limit to the 67 GHz 3 dB bandwidth of the photodiode leads to the conclusion that the combined O-E bandwidth is predominately carrier transit time limited. Assuming an average carrier drift velocity of 5.3^{x} 10^4 m/s in the InGaAs active layer [8] with 400 nm thickness, the calculated transit-limited bandwidth is ~74 GHz which matches the 67 GHz measured result fairly well. Additional improvements in speed could be accomplished by reducing the thickness of the active region [11], and thus reducing the transit time. However, this has the drawback of reducing the mode overlap with the active region and thus reducing responsivity.

The photo-generated microwave power from a 70 GHz sinusoidal beat tone is shown for both photodiode A and B in Fig. 7. The output power was measured with an E-band power

Optics EXPRESS

sensor and de-embedded from the 1.12 dB of loss from the E-band WR-12 waveguide probe. There is about 10~11 dB difference between the ideal output power and that measured. The discrepancy in power is attributed to high-frequency roll-off which was measured to be 4~5 dB at 70 GHz, and a 50% optical modulation depth in our optical system during measurement which corresponds to another 6 dB of power loss. The maximum saturation current is 9 mA at −5 V bias for PD A, and 6.5 mA for PD B.

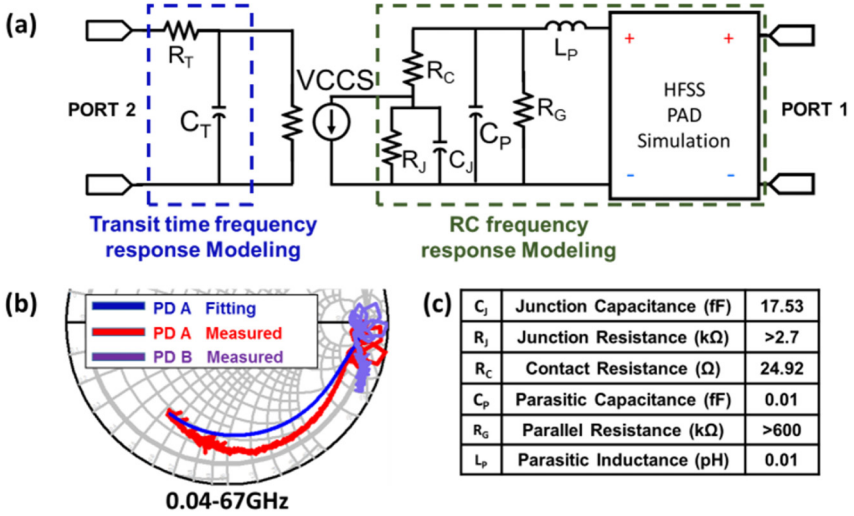

C_J	Junction Capacitance (fF)	17.53
R_J	Junction Resistance (kΩ)	>2.7
R_C	Contact Resistance (Ω)	24.92
C_P	Parasitic Capacitance (fF)	0.01
R_G	Parallel Resistance (kΩ)	>600
L_P	Parasitic Inductance (pH)	0.01

Fig. 6. (a) Photodiode equivalent-circuit-model. (b) Measured (blue and purple lines) and fitted (red line) S_{11} parameters from 40 MHz to 67 GHz under a fixed −3 V bias. Fitting was only done for the PD A due to difficulty in modeling the PD B. (c) Table with the values of the circuit elements used in the modeling process.

Photodiode A exhibits higher responsivity, higher saturated output current and power, and a nearly identical 3 dB roll-off point. Thus, it is the photodiode of choice for the microwave generator.

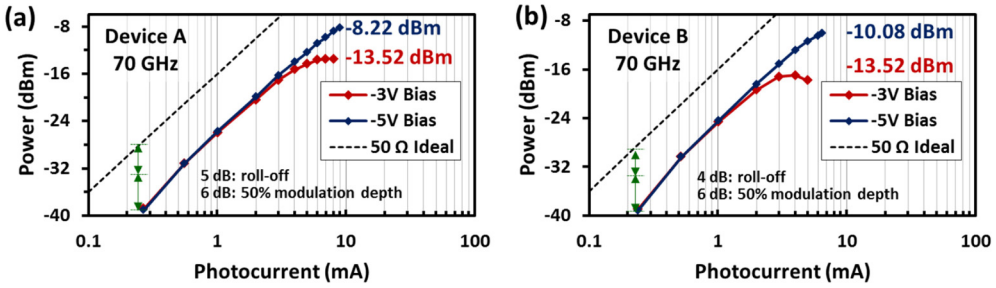

Fig. 7. The measured photo-generated MMW power of (a) device A and (b) device B vs. photocurrent under sinusoidal signal excitation and different reverse bias voltages (−3 and −5 V) at an operating frequency of 70 GHz and wavelength of 1550 nm. The solid line shows the ideal trace for a 100% modulation depth and 50 Ω load.

4. Laser structures and measurement

Two types of lasers were used in this chip. The first is a ring-bus-ring (RBR) laser which utilizes two ring filters in drop configuration in series and two teardrop reflectors. The second is a single-sided coupled-ring resonator (CRRx1) laser which utilizes a CRR mirror [12–15] on one side as both reflector and filter, and a teardrop reflector on the other side. A schematic of both types is shown in Fig. 8. Both lasers use ring filters of different circumference in order to

Optics EXPRESS

make use of the Vernier effect. Resistive heaters overlay the rings to provide active tuning of the wavelength. Ring circumferences of the RBR laser are 256 μm and 271 μm giving an expected tuning range greater than 40 nm. For the CRRx1 laser, the selected circumference values for Ring 1 and Ring 2 were 337 μm and 368 μm respectively, and the selected power coupling coefficient values for K_1, K_2, and K_3 are 2.25%, 2.25%, and 36% respectively.

The CRR mirror functions by coupling the light from the bus waveguide into Ring 2, which has a large coupling coefficient. Some of this light is also coupled into the second ring where it can couple back into the bus waveguide. This allows the light to reverse direction and to be filtered by two rings. A more detailed description of CRR mirror properties is found in [12] and [13]. The calculated function of the passive ring filters is shown in Fig. 9.

An optical photo of the two laser types is shown in Fig. 10. Wavelength tuning for both lasers was mapped out vs. ring heater power [Fig. 11]. The RBR laser had a tuning range of 42 nm and the CRRx1 laser had a tuning range of 21 nm. Maximum measured output power was 7.7 mW for the RBR laser and 10.5 mW for the CRRx1 laser as collected with an integrating sphere. The difference in power is due to the difference in mirror reflectivity.

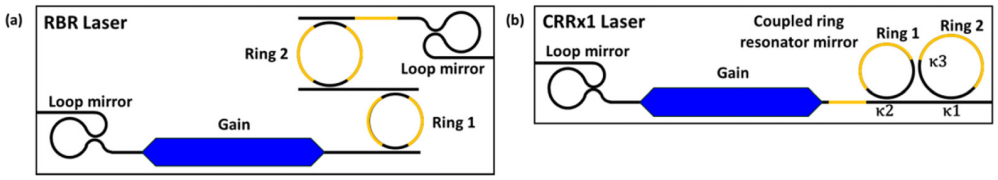

Fig. 8. Schematic of (a) the ring-bus-ring laser and (b) the one-sided coupled ring resonator laser.

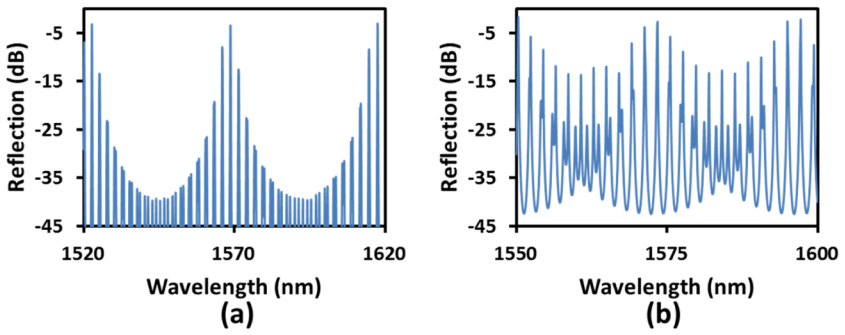

Fig. 9. Calculated filter function for (a) two passes through the rings of the RBR laser and (b) the CRR mirror of the CRRx1 laser mirror.

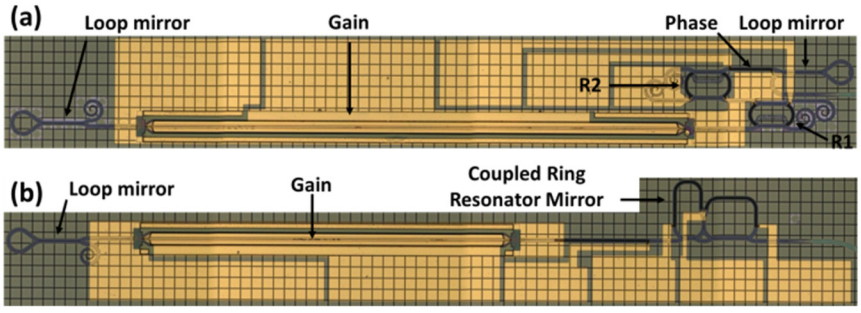

Fig. 10. Optical image of the completed (a) ring-bus-ring laser and (b) CRRx1 laser.

Optics EXPRESS

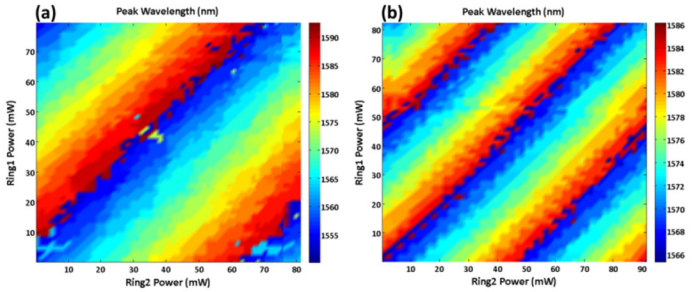

Fig. 11. Plot of peak wavelength vs. ring tuning power for (a) RBR laser and (b) CRRx1 laser.

The laser linewidths were tested using the delayed self-heterodyne method [16]. In this method the collected light is split into two arms. One arm is delayed by more than the coherence length. In this case we used 10 km of fiber. The other arm passes through an acousto-optic modulator which shifts the frequency by 100 MHz. When the light is brought back together on a photodiode and measured on an electrical spectrum analyzer (ESA), the resulting spectrum is double the linewidth of the laser. A schematic of the linewidth test setup is shown in Fig. 12 and plots of the measured spectra are shown in Fig. 13. Coincidentally, both the RBR laser and the CRRx1 achieved the same best linewidth, 148 kHz, which is a respectable result. For comparison, recent results of a widely tunable monolithically integrated external cavity laser in the O-band achieved 50 kHz best linewidth [17], which is only ~3 times lower than these integrated lasers. However, while the CRRx1 laser showed linewidths below 200 kHz across the tuning range, the RBR laser went as high as 280 kHz when tuning.

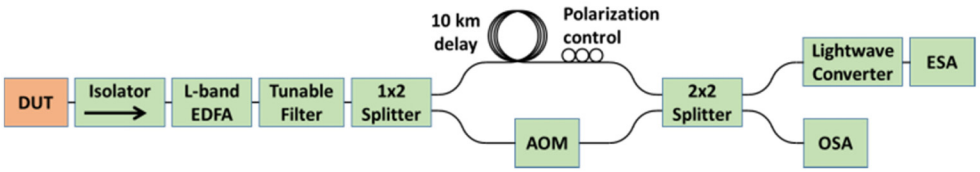

Fig. 12. Schematic of delayed self-heterodyne linewidth measurement setup.

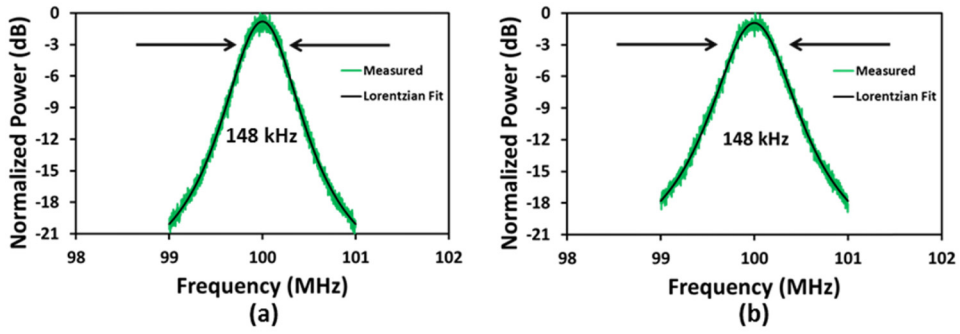

Fig. 13. Plots of measured linewidths for (a) RBR laser (148 kHz) and (b) CRRx1 laser (148 kHz).

Although both lasers showed a clear peak wavelength tuning map, the CRRx1 laser would often lase in multiple modes, making it more difficult to tune as desired. The RBR laser is much simpler to operate due to its consistent single frequency operation.

5. Photonic microwave generator measurement

The completed photonic microwave generator chip is shown in Fig. 14. Testing of the completed chip included 8-pin probe cards for each laser, and a 67 GHz ground-signal-ground

Optics EXPRESS

(GSG) probe for the photodiode. The electrical signal was measured using a Rhode and Schwarz 50 GHz FSU Spectrum Analyzer (ESA), and the optical signal was captured through a lensed fiber and monitored on a Yokogawa AQ6370C optical spectrum analyzer (OSA). Figure 15 shows a schematic of the test setup. Higher frequency measurements used an E-band WR-12 waveguide probe in conjunction with a Keysight E8486A E-band power sensor.

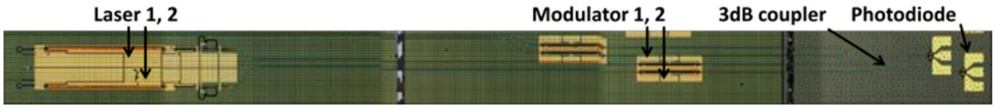

Fig. 14. Optical microscope image of the fully integrated photonic microwave generator chip.

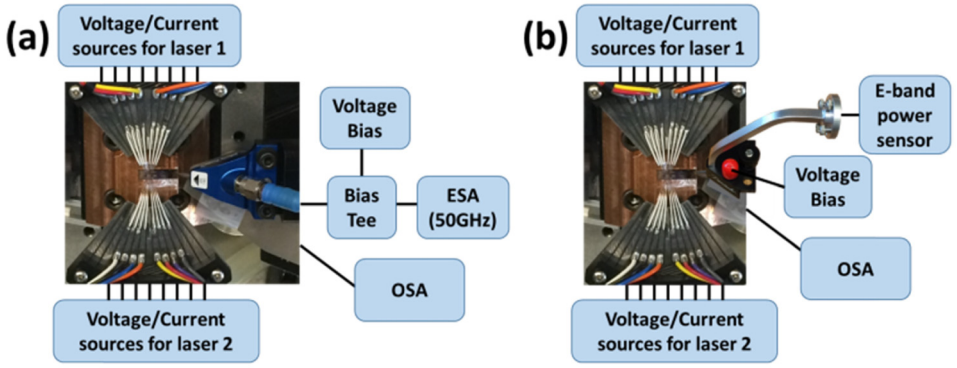

Fig. 15. Test setup for microwave generator chip (a) up to 50 GHz and (b) beyond 50 GHz.

Both the RBR and the CRRx1 lasers were used in the microwave generator. The CRRx1 was used for its higher output power, and the RBR laser was tuned to match it. A plot of the measured microwave power is shown in Fig. 16. By tuning one laser relative to the other the beat tone frequency is swept across from 1 to 112 GHz. The measured power roll-off does not correspond exactly with the photodiode roll-off, which is attributed to differences in laser power at different tuning settings. The optical spectra for the first 50 GHz are plotted in Fig. 17. It is notable that these results were accomplished without any off-chip amplification. In addition, compared with the MMW generator on a III-V platform [18], our demonstrated heterogeneously integrated silicon-III/V PIC has more advanced tunable laser structures, which could provide wider tuning range in optical central wavelengths (tens of nm vs. several nm) with a narrower linewidth (~0.25 vs. ~2 MHz) [19] and benefit the photo-generated beat signal up to the THz regime with acceptable phase noise. Furthermore, by combining the advanced fabrication process of a silicon photonic foundry and III-V active layers, a MMW photonic system-on-chip can be expected with more functionalities and larger scale for integration.

Optics EXPRESS

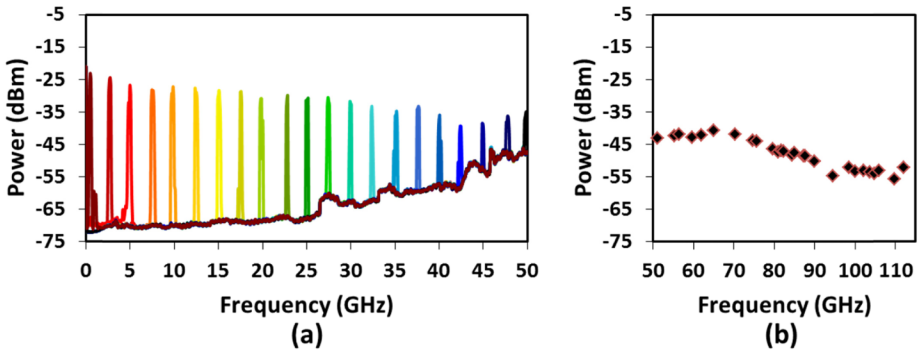

Fig. 16. Measured microwave signals (a) from 1 to 50 GHz on an ESA, and (b) from 50 to 112 GHz on an E-band power meter.

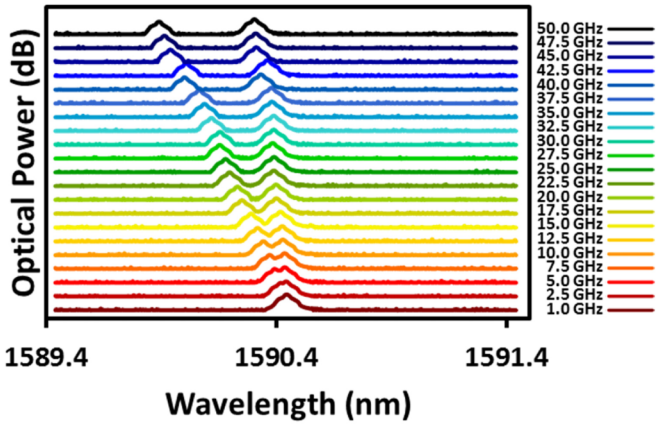

Fig. 17. Optical spectrum from fiber-coupled facet for microwave signals from 1 to 50 GHz.

6. Conclusions

A heterogeneously integrated silicon-III/V PIC was demonstrated including tunable lasers and p-i-n photodiode. By use of an ECPD structure and thick BCB layer for planarization, such a device can achieve 3-dB O-E bandwidth as wide as 65 GHz, a wide optical operation window (1520 to 1600 nm) with a reasonable internal responsivity (~0.4 A/W), and a high saturation current (9 mA) at 70 GHz operating frequency. Two ring-based tunable lasers were demonstrated. Tuning of 42 nm was demonstrated with mostly consistent SMSR for the RBR laser. Both lasers exhibit linewidths below 150 kHz. The photodiode and lasers were integrated to demonstrate on-chip microwave generation. Signals from 1 to 112 GHz were achieved.

Future improvements can be made to individual components. The RBR laser should be the laser of choice due to its simple operation and low linewidth. The output power can be raised by increasing mirror reflectivity and optimizing ring coupling through more precise processing, as well as adding a booster semiconductor optical amplifier after the laser. The speed and saturation power of the photodiode can be further improved by replacing the p-i-n PD with a UTC-PD structure.

This device shows that the heterogeneous silicon-InP platform is a viable option as a key component in MMW-over-fiber systems.

Funding

Keysight Technologies.